Effect of leading-edge curvature on the aerodynamics of insect wings

Shantanu S. Bhat [a,*], Mark C. Thompson [b]

[a] *School of Mechanical Engineering, University of Adelaide, Adelaide, SA 5005, Australia*
[b] *Fluids Laboratory for Aeronautical and Industrial Research (FLAIR), Department of Mechanical and Aerospace Engineering, Monash University, Clayton, VIC 8000, Australia*

ARTICLE INFO

ABSTRACT

The aerodynamic performance of an insect wing is largely dependent on the leading-edge vortex (LEV) on the wing formed during the rotational translation phase of its flapping motion. The geometry of the wing can directly influence the formation and strength of the LEV. The wing geometry is broadly defined by the aspect ratio and the radii of the wing's moment of inertia, which can be optimised to obtain the highest possible lift at a given Reynolds number. However, the shape of the leading edge can also affect the LEV and the tip vortex structure. A straight leading edge and a sharp wingtip can affect the spanwise vorticity flux responsible for a stable LEV, thereby affecting the lift and drag. To investigate this in the current study, the wing shape is initially approximated by the Beta function with a straight leading edge and is varied systematically by increasing the leading-edge curvature. The lift and power economy are observed to be enhanced with the leading-edge curvature. The reasons behind the lift enhancement are further investigated by analysing the LEV structures over the wings of various leading-edge curvatures. The curved leading edge is observed to enhance lift at both low as well as high Reynolds numbers relevant to insects.

1. Introduction

An increasing need for efficient micro-air vehicles (MAVs) has created a great interest in understanding insect-wing aerodynamics (Savage, 2015). This is because steady wings of the flyers of small sizes experience negligible lift due to very low inertia. A higher lift can be achieved by flapping the wings similar to insects. Motivated by this, several studies (e.g. Birch et al., 2004; Ansari et al., 2008; Shahzad et al., 2016; Bhat et al., 2019; Bhat et al., 2020) have been undertaken to maximise lift as well as power economy of insect-like wings.

Various geometrical and kinematic parameters have been found to influence wing performance. Wing aspect ratio, Reynolds number, Rossby number, and advance ratio are amongst the important parameters affecting the insect-wing aerodynamics (e.g. Dickson and Dickinson, 2004; Harbig et al., 2013; Wolfinger and Rockwell, 2014; Carr et al., 2015; Tudball Smith et al., 2017; Jardin and Colonius, 2018). The aspect ratio broadly describes the geometry of a wing, which is defined as the ratio of the wingspan to the mean wing chord ($AR = b/\bar{c}$). Recent studies have found that, for a hovering insect wing, the effects of aspect ratio, Reynolds number, and Rossby number are coupled (Harbig et al., 2013; Lee et al., 2016; Bhat et al., 2019). The individual and combined effects

of these parameters have been studied in detail and a polynomial model has been proposed (Bhat et al., 2019) to predict the lift coefficient of a rotating insect wing. This model can be used to maximise the lift coefficient for given Reynolds- and Rossby numbers of a flapping-wing MAV.

Most studies on wing shapes (e.g. Ansari et al., 2008; Wang et al., 2013; Nabawy and Crowther, 2016; Lee et al., 2016; Bhat et al., 2019) suggested that the wings with a larger area outboard experience higher lift and those with a larger area inboard experience higher power economy. These wings can be classified based on the Rossby number, which is defined by the ratio of the radius of the second moment of inertia to the mean wing chord ($Ro = r_2/\bar{c}$). Using the recommendations from previous studies, optimum AR and Ro can be chosen to achieve the best possible performance of a flapping-wing MAV in a designed flight regime. However, for chosen optimal AR and Ro, the wing shape can further be changed depending on the shape of the leading edge, which might have additional effects on the wing aerodynamics. Those effects have not been explored.

Insect wing aerodynamics is largely dependent on the leading-edge vortex (LEV) formed on a wing. The flapping motion of an insect wing during the simplified hovering stroke comprises two half-strokes, namely, the forward and backward strokes. The rotation of the wing

---

with approximately a constant angle of attack and a constant angular velocity constitutes a major part of a half-stroke, which is called the rotational translation, followed by the wing flip. During the rotational translation, the leading-edge vortex (LEV) formed by the air separating over the leading edge of the wing remains stably attached to the wing (Ellington et al., 1996; Eldredge and Jones, 2019). This stable LEV is responsible for the stable lift experienced by the wing during the rotational translation. Hence, many experimental and computational studies (e.g. Birch et al., 2004; Ozen and Rockwell, 2013; Harbig et al., 2013) have investigated a purely rotating wing to understand the aerodynamics during the rotational translation phase.

So far, it has been understood that an LEV is stabilised by the action of the Coriolis acceleration of the fluid, which transports the additional vorticity fed into the LEV from the leading edge to the wing tip (Lentink and Dickinson, 2009; Jardin, 2017). This results in a spanwise vorticity flux that merges the LEV into the tip vortex (TV). The merging of the LEV and TV might be affected by the shape of the leading edge and the wingtip, which might ultimately affect the lift acting on the wing. Some discussion on the effects of the overall wing shape and wing sweep on the LEV-TV dynamics can be seen in the literature (e.g. Taira and Colonius, 2009; Beem et al., 2012; Zhang et al., 2020). However, to our knowledge, the specific effects of the leading-edge curvature on the insect-wing aerodynamics have also not been explored systematically.

Therefore, the present work investigates the effects of the change in wing shape on aerodynamics by introducing leading-edge curvature. Direct numerical simulations of a rotating wing have been performed to represent the wing motion during the rotational translation. The leading-edge curvature has been changed systematically to observe the effects on the lift as well as the power economy of the wing. Furthermore, the flow structure around the wing has been analysed to investigate the reasons behind the lift enhancement obtained with a change in the leading-edge curvature.

2. Computational method

The computational method used in this study involves a model of a rotating wing at a constant angle of attack $\alpha = 45°$. The flow over the wing was simulated by directly solving Navier–Stokes equations in a non-inertial rotating frame of reference using the commercial code ANSYS CFX 20.1. This method has been previously used and validated by Harbig et al. (2013), Bhat et al. (2019) and Bhat et al. (2019). The detailed description of the wing geometry and kinematics is as follows.

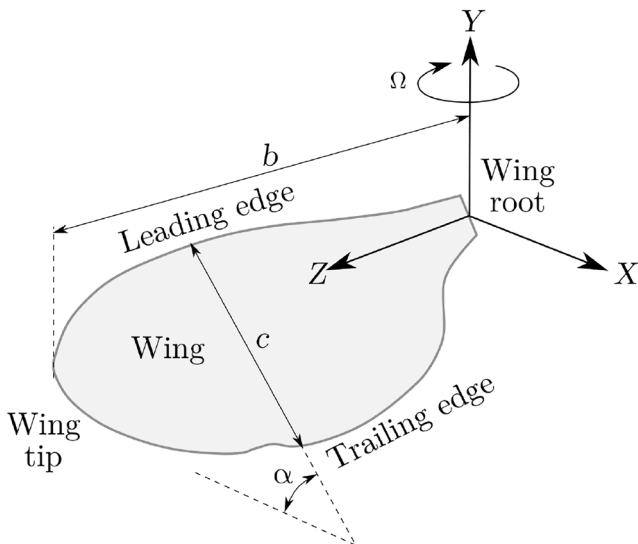The wing geometry was based on the fruit-fly wing planform with the

Fig. 1. Schematic of the rotating-wing geometry.

wingspan $b = 2.47$ mm and the aspect ratio $AR = 2.91$ (Zanker, 1990), as can be seen in Fig. 1. The span-based Rossby number for this wing planform was found to be $Ro_b = r_2/b = 0.57$. The wing of this shape was modelled as a rigid flat plate of thickness $t = 0.01b$. The wing was situated at the centre of a cylindrical domain of diameter $18b$ and height $48\bar{c}$. The fluid domain near the wing surface was meshed using triangular prism cells with a grid-spacing of $0.0145\bar{c}$. The remaining domain was meshed using an unstructured tetrahedral grid, resulting in, approximately, 8 million cells. The time step was chosen to be $0.00185T$, where T is the total simulation time. This corresponds to a total of 540 timesteps throughout the simulation.

The top and bottom flat surfaces of the cylindrical domain were modelled as openings. The cylindrical surface was modelled as a free-slip wall. The wing surfaces were modelled as no-slip walls. The motion of the wing was described by

$$\Omega\left(t\right) = \begin{cases} \frac{1}{2}\Omega\left[1 - \cos\left(\frac{\pi t}{0.084T}\right)\right], & 0 \leqslant t \leqslant 0.084T \\ \Omega, & 0.084T < t \leqslant T \end{cases} \quad (1)$$

i.e., the wing was accelerated from rest over the initial time $t = 0.084T$, followed by a constant angular velocity Ω that resulted in the span-based Reynolds number of $Re_{span} = U_t b/\nu = 520$, where U_t is the wingtip velocity and ν is the kinematic viscosity of the surrounding fluid. This is in the range of Reynolds numbers of fruit-fly wings, as have been reported by Ennos (1989) and Zanker and Götz (1990).

In contrast to chord-based definitions in the studies in the past, the span-based definition has been used for the Reynolds- and Rossby numbers, as the recent studies show that the wingspan is more relevant to the LEV dynamics and it decouples the aspect-ratio effects (Harbig et al., 2013; Bhat et al., 2019; Bhat et al., 2019) on the wing aerodynamics. The LEV was observed to form and grow until the rotation of $\sim 90°$ and stabilised in shape beyond this time, similar to that reported by Bhat et al. (2018). Such growth and stabilisation of the LEV has been well known in the case of rotating insect-wing planforms and the stable state has been referred to as the quasi-steady state (Poelma et al., 2006). The simulations were stopped when the wing rotated by $270°$, such that the starting wake could not interfere with the developed flow structure on the wing.

3. Wing shapes and modifications

As the effects of AR, and Ro_b on the wing aerodynamics are coupled (Bhat et al., 2019; Bhat et al., 2019), these parameters were decided to be maintained constant throughout the study to avoid the coupled effects. In fact, for $Re_{span} = 520$, the values of $AR = 2.91$ and $Ro_b = 0.57$ were found to be optimum for achieving the highest possible lift coefficient (Bhat et al., 2019). With the fixed AR and Ro_b, the wing shapes were varied by the chord-wise redistribution of the wing area, which resulted in the modified leading-edge curvature.

The base wing planform was derived using the Beta function. Ellington (1984) has studied shapes of various insect wings and proposed the spanwise distribution of wing chord using the Beta function as follows:

$$c\left(r\right) = \bar{c}\frac{\hat{r}^{p-1}(1 - \hat{r})^{q-1}}{\beta(p, q)}, \quad (2)$$

where

$$\beta\left(p, q\right) = \int_0^1 \hat{r}^{p-1}(1 - \hat{r})^{q-1}\mathrm{d}\hat{r}, \quad \hat{r} = r/b,$$
$$p = \hat{r}_1\left(\frac{\hat{r}_1(1 - \hat{r}_1)}{\hat{r}_2^2 - \hat{r}_1^2} - 1\right), \quad \text{and} \quad q = p\frac{(1 - \hat{r}_1)}{\hat{r}_1}. \quad (3)$$

Here, r is the spanwise distance from the wing root, b is the wingspan,

and r_1 and r_2 are the radii of the first and second moments of the wing area, respectively. Throughout this study, the values, $\hat{r}_1 = 0.52$ and $\hat{r}_2 = 0.57$, and the wing area $S = 2.095$ mm^2, were maintained to be constant, which were the same as the fruit-fly wing planform. Therefore, the spanwise distribution of the wing chord $[c(r)]$ remained the same across various investigated wing geometries. The shape of the leading edge was modified by providing the curvature, as discussed in the subsequent sections. This altered the trailing edge shape to maintain the same $c(r)$.

4. Effects of the leading-edge curvature

The effects of the leading-edge curvature were investigated in two phases. In the first phase, the original fruit-fly wing planform was modified. In the second phase, the Beta function was used to construct the wing planform and it was modified systematically, increasing the leading-edge curvature.

4.1. Effect on the fruit-fly wing planform

The original fruit-fly wing planform (FF Wing) has a curved leading edge. Using the same values of $c(r)$, a new planform was constructed with a straight leading edge, as can be seen in Fig. 2(a). The timetraces of the lift coefficient (C_L) and drag coefficient (C_D) of these wings are compared in Figs. 2(b) and 2(c), respectively. Here, C_L and C_D are calculated based on the wingtip velocity U_t and wing area S, such that

$$C_L = \frac{L}{0.5\rho U_t^2 S} \quad \text{and} \quad C_D = \frac{D}{0.5\rho U_t^2 S}, \quad (4)$$

where ρ is the fluid density, and L and D are the lift and drag, respectively.

It can be seen that the values of C_L and C_D rise rapidly during the initial acceleration of the wing and reach peaks near $t/T \sim 0.085$. Once the wing achieves a constant angular velocity, the values of C_L and C_D fluctuate by a smaller amount and stabilise beyond $t/T = 0.7$. Stable values of C_L and C_D are obtained after the LEV on the wing is stabilised, as has been discussed earlier by Bhat et al. (2019). Hence, the average

values of C_L and C_D, i.e. $\overline{C}_L$ and $\overline{C}_D$, respectively, are extracted over the final 25% time of the wing rotation.

The values of C_L of the FF wing is observed to be slightly greater than that of the modified FF wing with a straight edge. However, the difference between their C_D values is negligible. Moreover, the performance of a wing constructed using the Beta function with a straight edge (BetaFF0) was also compared. The C_L time-traces of the modified FF wing and the BetaFF0 wing were almost identical, with a very small difference.

A quantitative comparison of the mean values of the lift and drag coefficients for the three wings is shown in Table 1. $\overline{C}_L$ of the FF wing is higher by $\sim 2\%$ than that of the modified FF wing. However, the difference between their $\overline{C}_D$ values is $\sim 0.5\%$. The BetaFF0 wing has the lowest $\overline{C}_L$ and $\overline{C}_D$ amongst the three wings. It should be noted that this difference in the values of $\overline{C}_L$ and $\overline{C}_D$ may not be picked up by experimental investigations due to uncertainties involved in force measurements.

Various studies use rectangular wings (e.g. Carr et al., 2015; Kruyt et al., 2015; Phillips et al., 2017), due to their simple design, to investigate vortical structures over the wings. Hence, for a ready comparison of wing performance, a rectangular wing of $AR = 2.91$ was rotated about its root at $Re_{span} = 520$. The value of Ro_b for a rectangular wing is 0.577, which is close to that of a fruitfly wing. The values of $\overline{C}_L$ and $\overline{C}_D$ for the rectangular wing have been included in Table 1. $\overline{C}_L$ for the rectangular wing is indeed close to that of the BetaFF0 wing, although somewhat less than that for the FF wing. The reason behind the higher

Table 1
Comparison of the aerodynamic performance of the FF, modified FF, BetaFF0, and rectangular wings. The values are averaged over the final 25% of the simulation time.

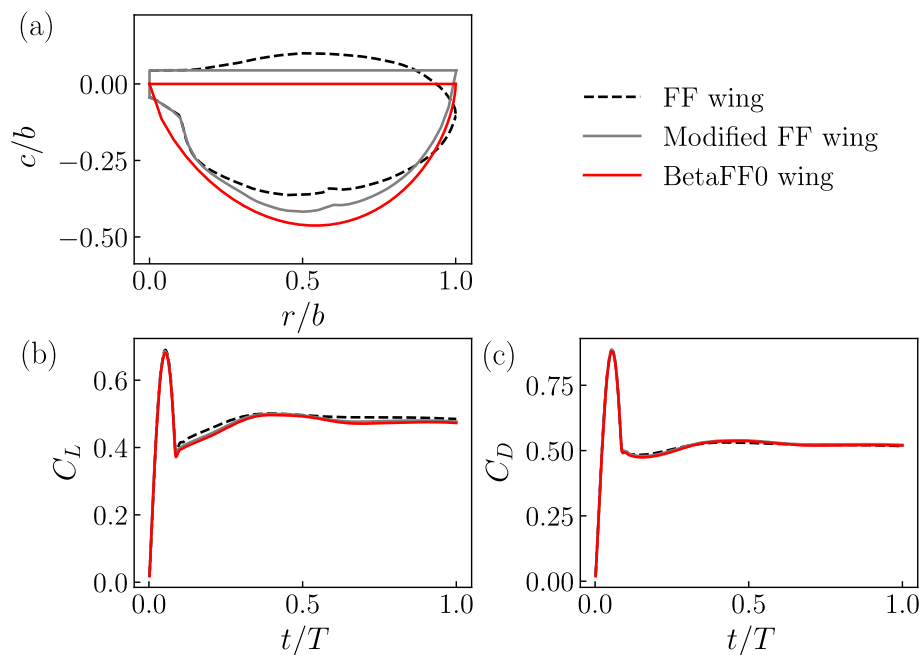| Wing	$\overline{C}_L$	$\overline{C}_D$
FF wing	0.488	0.521
Modified FF wing	0.479	0.524
BetaFF0 wing	0.474	0.52
Rectangular wing	0.473	0.515

Fig. 2. The comparison of wing planforms in subfigure (a) shows the original fruit-fly wing (FF wing), the modified FF wing with a straight leading edge (Modified FF wing) and the shape defined by the Beta function with a leading edge (BetaFF0). The timetraces of C_L and C_D of these wings are compared in subfigures (b) and (c), respectively.

$\overline{C}_L$ with a curved leading edge is explored in the following subsection.

4.2. Effect on the Beta wing planforms

In order to observe the effect of wing curvature on the wing aerodynamics, the wing shape was systematically varied with increasing curvature. The wing area distribution was chosen to be based on the Beta function, as described earlier. The BetaFF0 wing, which had a straight leading edge, was selected as the baseline case. While modifying the shape of the leading edge, its midpoint was moved up and the wing tip was moved down, both by the equal amount y_c. The inner half of the leading edge was defined by an ellipse of the semi-minor axis of $4y_c$. The outer half of the leading edge was defined by an ellipse of the semi-minor axis of $2y_c$. This may be similar to the LE in the four-ellipse wing model of Ansari et al. (2008). The trailing edge shape was adjusted to maintain the same $c(r)$ as defined by the Beta function.

The curvature of the leading edge can be characterised by the normalised mean curvature of the inner half of the leading edge. Averaging over the outer half of the leading edge was avoided as the sharp curvature near the wingtip, provided to the wing of a lower y_c to achieve a smooth leading-edge–wingtip transition, can result in a misleading number. The normalised curvature of a point on an ellipse is given by

$$\kappa^* = \frac{A^*B^*}{\left(A^{*2}\sin^2\theta + B^{*2}\cos^2\theta\right)^{3/2}}, \quad (5)$$

where $A^* = A/b$ and $B^* = B/b$ are, respectively, the normalised semi-major and semi-minor axes of the ellipse, and θ is the angle made by the vector joining the centre of the ellipse and the point on the ellipse with respect to the major axis.

The leading-edge curvature was varied to create 3 different wings with $y_c/b = 0.05$, 0.1, and 0.15, as can be seen in Fig. 3. Those resulted in $\kappa^* = 0.66$, 1.15, and 1.45, respectively. For simplicity, those wings were named BetaFF1, BetaFF2, and BetaFF3, respectively. Varying the y_c/b beyond 0.15 resulted in a concave shape of the trailing edge near the wingtip. Hence, larger values of y_c/b were avoided. Interestingly, the shape of the BetaFF2 wing was observed to be closer to that of the FF wing, as can be seen in Fig. 3.

The values of $\overline{C}_L$ and $\overline{C}_D$ were extracted for these wings. Moreover, the power economy was calculated as $PE = \overline{C}_L/\overline{C}_P$, where $\overline{C}_P$ is the coefficient power required for rotating the wing averaged over $0.75 \leqslant t/T \leqslant 1$. C_P was calculated by normalising the aerodynamic torque acting along the Y-axis (τ_y), i.e.

$$C_P = \frac{\tau_y}{0.5\rho U_t^2 Sb}. \quad (6)$$

The power required to rotate the wing is directly dependent on $\overline{C}_D$ since the torque τ_y is required to overcome the drag. The values of $\overline{C}_L$, $\overline{C}_D$, and PE for the four wings are compared in Table 2.

It can be seen that $\overline{C}_L$ increases with the amount of leading-edge curvature. BetaFF3 has the highest $\overline{C}_L$ amongst the four variants and it is 4.2% higher than that of BetaFF0. Interestingly, $\overline{C}_D$ increases by a smaller amount than $\overline{C}_L$. This results in an improvement in PE. It should be noted that even a small improvement in the performance of biological flyers is significant. Moreover, this improvement in the present cases was observed after choosing the most optimum geometrical parameters of the wing, i.e. AR and $\hat{r}_2$. Therefore, the additional enhancement in the lift provided by the leading-edge curvature is remarkable.

The reasons behind the improvement in the wing performance with the leading-edge curvature were further investigated by extracting the vortical structures over the wings at $t/T = 1$, as shown in Fig. 4. Here, the vortical structures have been shown using the isosurfaces of the constant Q-criterion (Hunt et al., 1988) coloured using the normalised helical density ($-\mathbf{u}^* \cdot \boldsymbol{\omega}^*$), where $\mathbf{u}^* = u/U_t$ is the normalised velocity and $\boldsymbol{\omega}^* = \omega b/U_t$ is the normalised vorticity. The helical density, or the scalar product of $\mathbf{u}^*$ and $\boldsymbol{\omega}^*$, serves as an indicator of the vorticity flux on the primary axis of a vortex (Moffatt, 1969; Bross and Rockwell, 2014; Van de Meerendonk et al., 2018). In the present work, the negative sign is used to represent the positive outward vorticity flux on the LEV axis, where the LEV has, primarily, negative vorticity.

As can be seen in Fig. 4, the LEV and TV appear to be distinct vortices, joined at the wingtip of BetaFF0. However, with an increase in the leading-edge curvature, the LEV merges smoothly into the TV. Furthermore, the LEV over BetaFF0 shows larger magnitudes of the inward helical density, shown by the blue colour, near the wingtip region. With a curved leading edge, BetaFF3 shows lower inward helical density. A trail of vorticity is observed to be left in the wake from near the tip vortex. In the case of BetaFF0, this trail appears to be detached from the LEV-TV system due to the lower magnitudes of the vorticity flux. The curved leading edge in BetaFF2 and BetaFF3 contributes to higher outward vorticity flux, showing the LEV-TV system to be connected with the trailing vortex. It should be noted that the apparent detachment of the trailing vortex is subjective to the choice of the Q values. However, this represents the lower magnitudes of vorticity being fed from the LEV compared to those with the curved leading edges, as shown quantitatively in Fig. 5. Furthermore, the normalised pressure (p^*) distribution on the four wings' suction surface is shown in Fig. 4. BetaFF3 shows slightly higher magnitudes of suction near the leading edge than the other wings.

The temporal development of the LEV-TV structure and the vorticity flux were investigated, as shown in Fig. 5. Here, the mean vorticity flux through the LEV ($\overline{-\mathbf{u}^* \cdot \boldsymbol{\omega}^*}_{LEV}$) was extracted over various spanwise cross-sections of the LEV and at various time steps. For both BetaFF0 and BetaFF3, the values of $\overline{-\mathbf{u}^* \cdot \boldsymbol{\omega}^*}_{LEV}$ are higher initially, at $t/T = 0.17$, and reduce in later timesteps. At $t/T = 0.17$, the peak vorticity flux in BetaFF0 is observed near $r/b = 0.55$ and that in BetaFF3 is observed near $r/b = 0.7$. The more outboard vorticity flux in BetaFF3 can be attributed to the smooth merging of the LEV into TV, as shown in Fig. 5 (c). With more rotation of the wing, the peak shifts inboard. Consequently, at $t/T = 1$, BetaFF0 shows the peak vorticity flux near $r/b =$
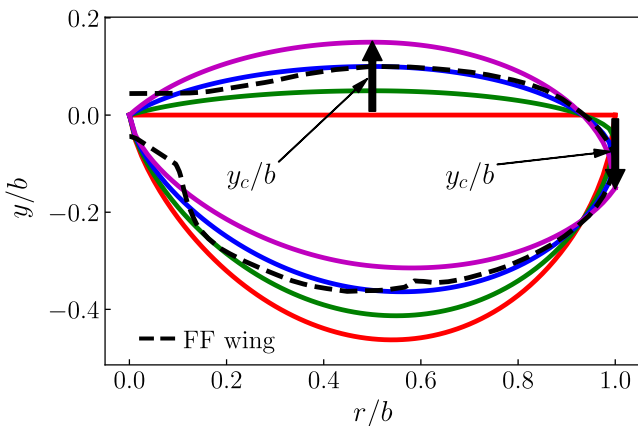

Fig. 3. Four wings are obtained using the beta function with various leading-edge curvature. The red, green, blue, and magenta colours represent the outlines of the wings BetaFF0, BetaFF1, BetaFF2, and BetaFF3, respectively.

Table 2

Comparison of $\overline{C}_L$, $\overline{C}_D$, and PE is shown for wings of various leading-edge curvatures rotating at $Re_{span} = 520$. The parameter κ^* represents the LE curvature.

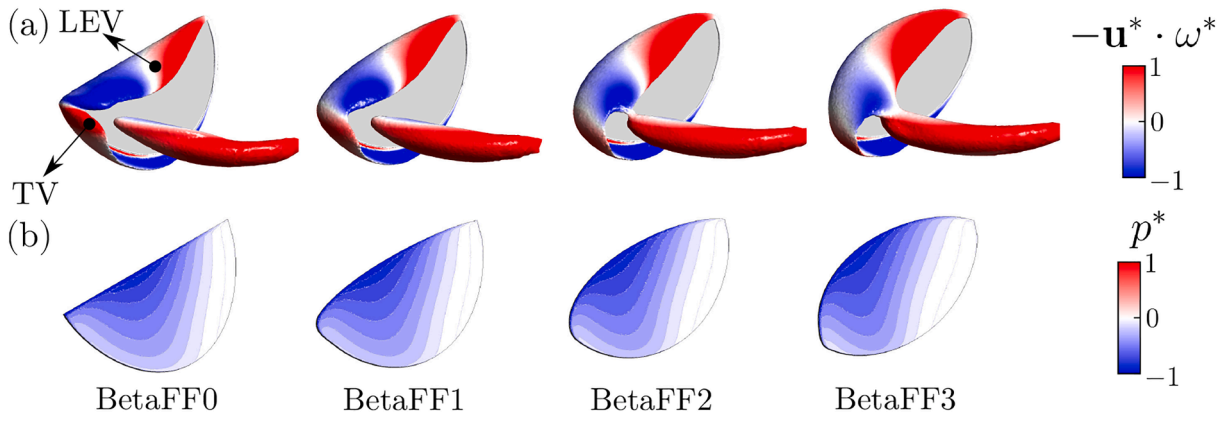| Wing	y_c/b	κ^*	$\overline{C}_L$	$\overline{C}_D$	PE
BetaFF0	0	0	0.474	0.520	0.307
BetaFF1	0.05	0.66	0.484	0.523	0.311
BetaFF2	0.1	1.15	0.488	0.523	0.312
BetaFF3	0.15	1.45	0.494	0.526	0.312

Fig. 4. The comparison shows (a) the vortical structures and (b) the p^* contours on the wing suction side, between wings of various LE curvatures. The vortical structures are shown by the isosurfaces of the constant Q criterion and coloured by the normalised helical density $-\mathbf{u}^* . \omega^*$). The wing orientation is the same as that shown in Fig. 1.
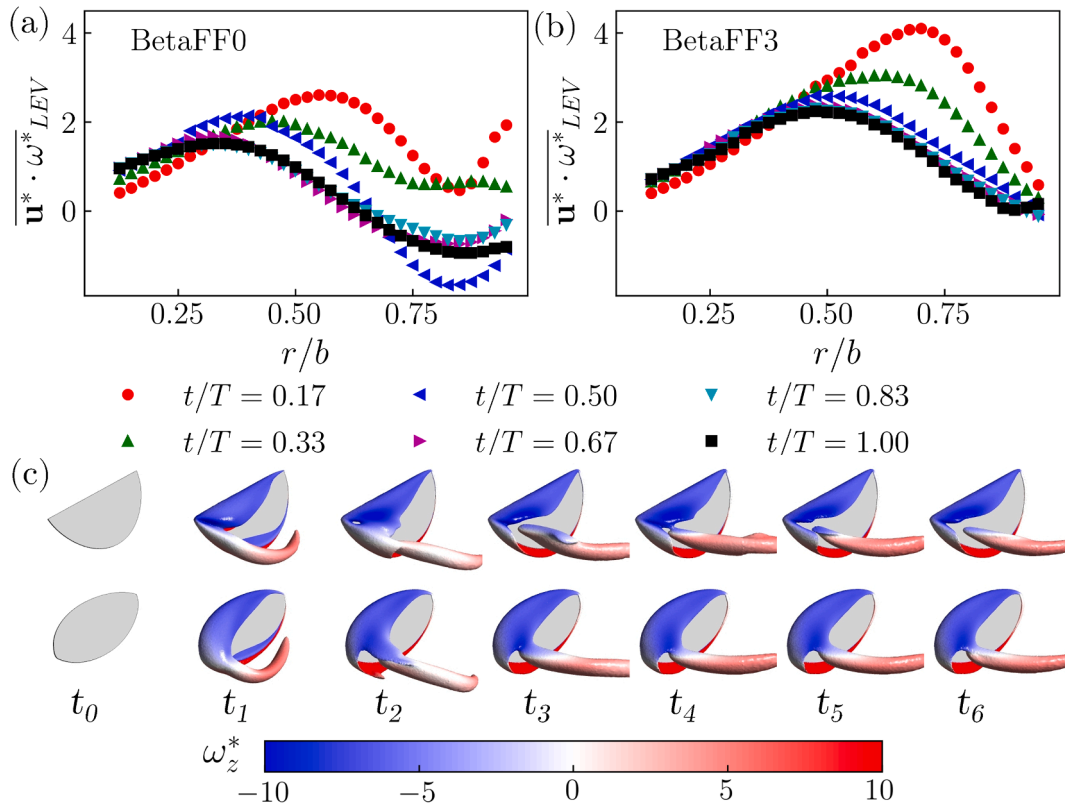

Fig. 5. The mean vorticity flux through the LEV at various spanwise cross-sections is shown at various timesteps for (a) BetaFF0 and (b) BetaFF3 wings. The vortical structures over these wings at the respective timesteps are shown in (c) using the constant Q criterion, coloured using ω_z^*. The first row in subfigure (c) shows the LEV evolution over BetaFF0 wing, whereas the second row shows that over BetaFF3 wing. The timesteps $t_0, t_1, t_2, t_3, t_4, t_5$, and t_6 correspond to the normalised time t/T of 0, 0.17, 0.33, 0.5, 0.67, 0.83, and 1, respectively.

0.35, whereas BetaFF3 shows it near $r/b = 0.5$.

Moreover, BetaFF0 shows a negative vorticity flux in the outboard region, whereas BetaFF3 maintains a positive vorticity flux throughout the wingspan. The higher vorticity flux allowed by the curved leading edge in BetaFF3 created a larger suction, which resulted in a higher $\overline{C}_L$. Interestingly, the higher suction was created closer to the leading edge and above the wing, rather than in the wake region. Hence, the force magnitude increased more along the Y-axis than in the X-axis. Therefore, the increase in $\overline{C}_L$ was found to be more than that in $\overline{C}_D$, as has been shown in Table 2. Overall, the curved leading edge helped enhance the power economy of the wing.

In the present work, all the wings were rotated about the axis passing through the root of their leading edges, following the practical arrangement in MAV wings. However, this causes a slight difference in the chordwise location of the wing centroid across various wing shapes, resulting in a slightly different polar moment of area. One way of maintaining the constant polar moment of area is to offset the wing's rotation axis along the chordwise direction. This was implemented in few chosen cases to verify the validity of the results after isolating the effects of the polar moment. The resulting values of $\overline{C}_L$ are shown in Fig. 6, where the radius of the polar second moment of area, i. e. polar $\hat{r}_2$ has been matched to that of the FF wing.
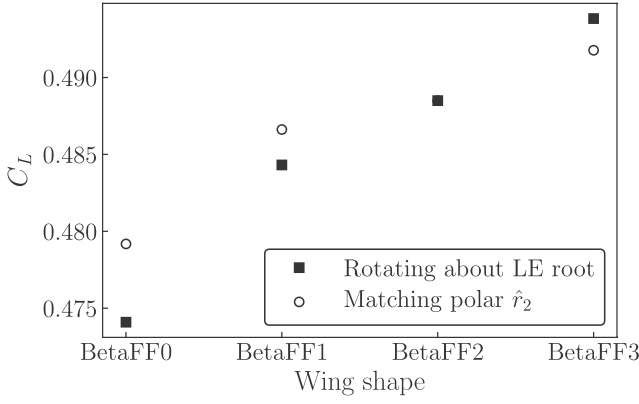
Fig. 6. Change in the values of $\overline{C}_L$ for wings from BetaFF0 to BetaFF3 with increasing leading-edge curvature. The values change slightly after matching the polar $\hat{r}_2$.

The figure shows that the values of $\overline{C}_L$ changed slightly after adjusting the polar $\hat{r}_2$. The improvement in $\overline{C}_L$ with increasing k^* is slightly less compared to the wings rotating about the root of the leading edge. However, the values still show an increasing trend, highlighting the fact that the leading-edge curvature does have a positive effect on the lift enhancement even after isolating the effects of the location of the centroid.

The other way of maintaining the constant polar $\hat{r}_2$ and rotating about the same wing root might require a different strategy for designing the wing curvature, which may be explored in a future study. The location of the pitching axis might also have additional effect on performance of a flapping wing, as has been discussed by Wang et al. (2017). However, the present work focuses on the pure rotational motion of the wing. Hence, pitching effects may also be explored in future work.

4.3. Effect of curved LE at higher Re

The current investigation was performed primarily at $Re_{span} = 520$,

as described earlier. However, the LEV structure on a wing is highly dependent on the span-based Reynolds number (Birch et al., 2004). The LEV at higher Re_{span} is stronger, more compact, and may result in a dual-LEV structure (Lu et al., 2006) followed by a vortex burst to form non-coherent structures in the wake, as can be seen in Figs. 7(e–f). Hence, the performance of the wings of various leading-edge curvatures was also investigated at $Re_{span} = 6930$. This corresponds to a typical Reynolds number for crane flies (Weis-Fogh, 1973). The computational parameters for the spatial and temporal discretisation were maintained to be the same as those for the lower Re_{span}. The convergence of the same model has been validated by Harbig et al. (2013) for a range of Reynolds numbers, up to $Re = 1500$, where Re is based on the velocity at the radius of gyration and the wing chord. In terms of the span-based Reynolds number, the method is validated for the Reynolds numbers of up to $Re_{span} = 7660$. Table 3 shows the comparison of $\overline{C}_L$, $\overline{C}_D$, and PE for BetaFF0, BetaFF1, BetaFF2, and BetaFF3 rotating at $Re_{span} = 6930$.

It should be noted that, in this case, both $\overline{C}_L$ and $\overline{C}_D$ increase by a similar amount, resulting in a negligible change in the power economy. The reason behind this was further investigated by comparing the normalised pressure contours on a spanwise plane, passing through the midpoint of the wingspan, as shown in Figs. 7(a–b). The LEV at this Reynolds number splits into two co-rotating vortices, called the dual LEVs. The stronger split LEV moves downward in the chordwise direction. In Figs. 7(a–b), the stronger suction is observed to be at the core of the secondary LEV, which is slightly away from the leading edge. Therefore, the increase in the suction in BetaFF3 due to the curved leading edge contributes equally to the $\overline{C}_L$ and $\overline{C}_D$. Nevertheless, the

Table 3
Comparison of $\overline{C}_L$, $\overline{C}_D$, and PE is shown for wings of various leading-edge curvatures (κ^*) rotating at $Re_{span} = 6930$.

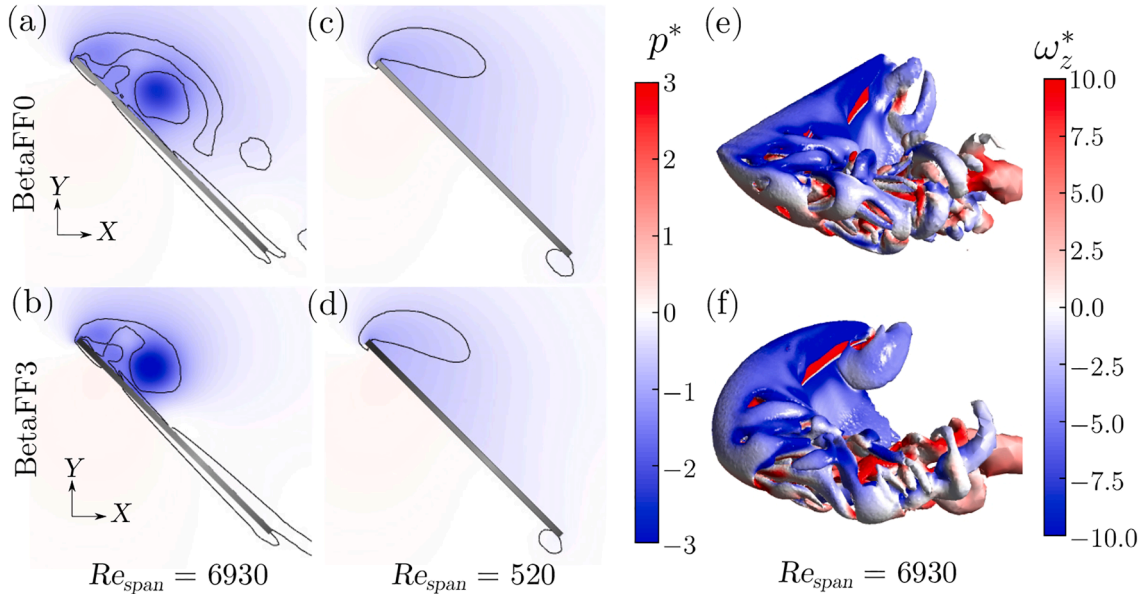| Wing	κ^*	$\overline{C}_L$	$\overline{C}_D$	PE
BetaFF0	0	0.567	0.533	0.361
BetaFF1	0.66	0.589	0.550	0.361
BetaFF2	1.15	0.595	0.554	0.361
BetaFF3	1.45	0.598	0.556	0.360

Fig. 7. The normalised pressure (p^*) contours around (a) BetaFF0 and (b) BetaFF3 at $Re_{span} = 6930$ are compared on a plane passing through the midpoint of the wingspan. The black lines represent the vortices identified by the constant Q criterion. The same contours on a midplane for BetaFF0 and BetaFF3 wings at $Re_{span} = 520$ have been shown in (c) and (d), respectively. The vortical structures over BetaFF0 and BetaFF3 wings are shown by isosurfaces of the constant Q criterion coloured by ω_z^* in (e) and (f), respectively.

value of $\overline{C_L}$ is found to be improved by 5.5% in BetaFF3 compared to that in BetaFF0. This improvement is slightly higher than that at lower Re_{span}. Overall, the curved leading edge is found to improve $\overline{C_L}$ irrespective of the Reynolds number. Figs. 7(c) and 7(d) show the normalised pressure contours over the same plane for BetaFF0 and BetaFF3, respectively, rotating at $Re_{span} = 520$. At this lower Re_{span}, the dual LEV structure is not observed. The lower magnitudes of pressure are also evident, which are due to the lower suction developed by the weaker spanwise vorticity flux.

While biologically-based structural and maintenance considerations may play a part in maximum leading-edge curvatures seen in insects, the same do not necessarily constrain artificial wings. The present study suggests that a higher leading-edge curvature can provide a lift advantage over biomimetic-based wing planforms. Therefore, these results might be useful, particularly to the designers of insect-like MAVs, to enhance the performance of their flyers for an efficient flight. The leading-edge curvature might also be applied to the wing shapes obtained using various shape-optimisation studies, such as those of Ghommem et al. (2014) and Bhat et al. (2019), for better performance.

5. Conclusions

A stable leading-edge vortex (LEV), stabilised by the spanwise vorticity transport during the rotational translation phase of the flapping motion, is responsible for the stable and higher lift observed in insects compared to their fixed-wing counterparts. The LEV structure and the resulting lift can be affected by the wing shape. Broadly, the wing shape can be defined by its aspect ratio (AR) and the normalised radius of the second area moment of inertia ($\widehat{r}_2$). However, these parameters are insufficient in determining the shape of the leading edge. A curved leading edge and wingtip can augment the spanwise vorticity flux, which may enhance the lift coefficient of the wing.

In this study, the effects of the leading-edge curvature were investigated systematically by numerically simulating the flow over rotating wings of various curvatures. The base wing was defined using the Beta function with a straight leading edge. The leading-edge curvature was varied by changing the value of the parameter y_c that represents the deviation of the mid-point of the leading edge with respect to its position in the straight edge. The values of AR, $\widehat{r}_2$, and Reynolds number were chosen to be the same as of a fruit fly wing. The lift coefficient and power economy of the wing were observed to improve with increasing leading-edge curvature. A detailed analysis showed that the curved leading edge contributed to an increased vorticity flux through the LEV, resulting in a higher suction created beneath the LEV. This was responsible for the higher lift observed on the wing with a curved leading edge. The drag was found to be less affected as the increase in the suction magnitude was more near the leading edge and above the wing. The same wings, when rotated at a higher Reynolds number, showed an increase in the lift as well as drag due to the leading-edge curvature. Therefore, the power economy remained unaffected by the leading-edge curvature at the higher Reynolds number. Nevertheless, the curved leading edge improved the lift irrespective of the Reynolds number.

The results might be of great interest to the designers of the flapping-wing micro-air vehicles to improve the performance of their flyers. The leading-edge curvature is shown to be an important geometrical parameter responsible for the aerodynamic performance of insect wings and the wings in similar applications.

CRediT authorship contribution statement

Shantanu S. Bhat: Conceptualization, Methodology, Formal analysis, Investigation, Writing - original draft. **Mark C. Thompson:** Conceptualization, Formal analysis, Project administration, Writing - original draft, Funding acquisition.

Declaration of Competing Interest

The authors declare that they have no known competing financial interests or personal relationships that could have appeared to influence the work reported in this paper.

Acknowledgements

References

Ansari, S.A., Knowles, K., Zbikowski, R., 2008. Insectlike flapping wings in the hover. Part I: Effect of wing kinematics. J. Aircraft 45, 1945–1954.

Ansari, S.A., Knowles, K., Zbikowski, R., 2008. Insectlike flapping wings in the hover. Part II: Effect of wing geometry. J. Aircraft 45, 1976–1990.

Beem, H.R., Rival, D.E., Triantafyllou, M.S., 2012. On the stabilization of leading-edge vortices with spanwise flow. Exp. Fluids 52, 511–517.

Bhat, S.S., Zhao, J., Sheridan, J., Hourigan, K., Thompson, M.C., 2018. The leading-edge vortex on a rotating wing changes markedly beyond a certain central body size. R. Soc. Open Sci. 5, 172197.

Bhat, S.S., Zhao, J., Sheridan, J., Hourigan, K., Thompson, M.C., 2019. Aspect ratio studies on insect wings. Phys. Fluids 31, 121301.

Bhat, S.S., Zhao, J., Sheridan, J., Hourigan, K., Thompson, M.C., 2019. Evolutionary shape optimisation enhances the lift coefficient of rotating wing geometries. J. Fluid Mech. 868, 369–384.

Bhat, S.S., Zhao, J., Sheridan, J., Hourigan, K., Thompson, M.C., 2019. Uncoupling the effects of aspect ratio, Reynolds number and Rossby number on a rotating insect-wing planform. J. Fluid Mech. 859, 921–948.

Bhat, S.S., Zhao, J., Sheridan, J., Hourigan, K., Thompson, M.C., 2020. Effects of flapping-motion profiles on insect-wing aerodynamics. J. Fluid Mech. 884, A8.

Birch, J.M., Dickson, W.B., Dickinson, M.H., 2004. Force production and flow structure of the leading edge vortex on flapping wings at high and low Reynolds numbers. J. Exp. Biol. 207, 1063–1072.

Bross, M., Rockwell, D., 2014. Flow structure on a simultaneously pitching and rotating wing. J. Fluid Mech. 756, 354–383.

Carr, Z.R., DeVoria, A.C., Ringuette, M.J., 2015. Aspect-ratio effects on rotating wings: circulation and forces. J. Fluid Mech. 767, 497–525.

Dickson, W.B., Dickinson, M.H., 2004. The effect of advance ratio on the aerodynamics of revolving wings. J. Exp. Biol. 207, 4269–4281.

Eldredge, J.D., Jones, A.R., 2019. Leading-edge vortices: mechanics and modeling. Annu. Rev. Fluid Mech. 51, 75–104.

Ellington, C.P., 1984. The aerodynamics of hovering insect flight. II. Morphological parameters. Philos. Trans. R. Soc. B: Biol. Sci. 305, 17–40.

Ellington, C.P., van den Berg, C., Willmott, A.P., Thomas, A.L.R., 1996. Leading-edge vortices in insect flight. Nature 384, 626–630.

Ennos, A.R., 1989. The kinematics and aerodynamics of the free flight of some diptera. J. Exp. Biol. 142, 49–85.

Ghommem, M., Collier, N., Niemi, A.H., Calo, V.M., 2014. On the shape optimization of flapping wings and their performance analysis. Aerosp. Sci. Technol. 32, 274–292.

Harbig, R.R., Sheridan, J., Thompson, M.C., 2013. Reynolds number and aspect ratio effects on the leading-edge vortex for rotating insect wing planforms. J. Fluid Mech. 717, 166–192.

Hunt, J.C.R., Wray, A.A., Moin, P., 1988. Eddies, streams, and convergence zones in turbulent flows. In: Center for Turbulence Research Report CTR-S88, pp. 193–208.

Jardin, T., 2017. Coriolis effect and the attachment of the leading edge vortex. J. Fluid Mech. 820, 312–340.

Jardin, T., Colonius, T., 2018. On the lift-optimal aspect ratio of a revolving wing at low Reynolds number. J. R. Soc. Interface 15, 20170933.

Kruyt, J.W., van Heijst, G.F., Altshuler, D.L., Lentink, D., 2015. Power reduction and the radial limit of stall delay in revolving wings of different aspect ratio. J. R. Soc. Interface 12, 20150051.

Lee, Y.J., Lua, K.B., Lim, T.T., 2016. Aspect ratio effects on revolving wings with Rossby number consideration. Bioinspiration Biomimetics 11, 056013.

Lentink, D., Dickinson, M.H., 2009. Rotational accelerations stabilize leading edge vortices on revolving fly wings. J. Exp. Biol. 212, 2705–2719.

Lu, Y., Shen, G.X., Lai, G.J., 2006. Dual leading-edge vortices on flapping wings. J. Exp. Biol. 209, 5005–5016.

Van de Meerendonk, R., Percin, M., Van Oudheusden, B.W., 2018. Three-dimensional flow and load characteristics of flexible revolving wings. Exp. Fluids 59, 1–22.

Moffatt, H.K., 1969. The degree of knottedness of tangled vortex lines. J. Fluid Mech. 35, 117–129.

Nabawy, M.R.A., Crowther, W.J., 2016. Optimum hovering wing planform. J. Theor. Biol. 406, 187–191.

Ozen, C.A., Rockwell, D., 2013. Flow structure on a rotating wing: effect of wing aspect ratio and shape. In 51st AIAA Aerospace Sciences Meeting. AIAA Paper 2013–676.

Phillips, N., Knowles, K., Bomphrey, R.J., 2017. Petiolate wings: effects on the leading-edge vortex in flapping flight. Interface Focus 7, 20160084.

Poelma, C., Dickson, W.B., Dickinson, M.H., 2006. Time-resolved reconstruction of the full velocity field around a dynamically-scaled flapping wing. Exp. Fluids 41, 213–225.

Savage, N., 2015. Aerodynamics: Vortices and robobees. Nature 521, S64–S65.

Shahzad, A., Tian, F.B., Young, J., Lai, J.C.S., 2016. Effects of wing shape, aspect ratio and deviation angle on aerodynamic performance of flapping wings in hover. Phys. Fluids 28, 111901.

Taira, K., Colonius, T., 2009. Three-dimensional flows around low-aspect-ratio flat-plate wings at low Reynolds numbers. J. Fluid Mech. 623, 187.

Tudball Smith, D., Rockwell, D., Sheridan, J., Thompson, M., 2017. Effect of radius of gyration on a wing rotating at low Reynolds number: a computational study. Phys. Rev. Fluids 2, 064701.

Wang, Q., Goosen, H., Keulen, F.V., 2013. Optimal hovering kinematics with respect to various flapping-wing shapes. In: International Micro Air Vehicle Conference and Flight Competition (IMAV2013). Toulouse, France.

Wang, Q., Goosen, J.F.L., van Keulen, F., 2017. Optimal pitching axis location of flapping wings for efficient hovering flight. Bioinspiration Biomimetics 12, 056001.

Weis-Fogh, T., 1973. Quick estimates of flight fitness in hovering animals, including novel mechanisms for lift production. J. Exp. Biol. 59, 169–230.

Wolfinger, M., Rockwell, D., 2014. Flow structure on a rotating wing: effect of radius of gyration. J. Fluid Mech. 755, 83–110.

Zanker, J.M., 1990. The wing beat of Drosophila melanogaster. I. Kinematics. Philos. Trans. R. Soc. B: Biol. Sci. 327, 1–18.

Zanker, J.M., Götz, K.G., 1990. The wing beat of Drosophila melanogaster. II. Dynamics. Philos. Trans. R. Soc. B: Biol. Sci. 327, 19–44.

Zhang, K., Hayostek, S., Amitay, M., Burtsev, A., Theofilis, V., Taira, K., 2020. Laminar separated flows over finite-aspect-ratio swept wings. J. Fluid Mech. 905, R1.